A complete vibroacoustic model for the nonlinear response of imperfect circular plates : application to sound synthesis

À Aragonès, Cyril Touzé, Stefan Bilbao, Michele Ducceschi

inter.noise
HAMBURG 2016

A complete vibroacoustic model for the nonlinear response of imperfect circular plates : application to sound synthesis

À. Aragonès[1], C. Touzé[2], S. Bilbao[3] and M. Duccheschi[4]
[1,2]IMSIA, ENSTA ParisTech, CNRS, CEA, EDF, Université Paris-Saclay, France
[3,4]University of Edinburgh, United Kingdom

ABSTRACT
A complete vibroacoustic model is presented in order to compute numerically the sound pressure generated by a thin circular plate vibrating with large amplitude motions. The vibratory part relies on a modal approach for the von Kármán thin plate equations. A special emphasis is put in this paper on the inclusion of a geometrical imperfection describing the shape of the circular plate, hence extending previous results for perfect plates to the generic case of imperfect plates and shallow shells. A conservative scheme is used in order to integrate in time the modal equations of motion for the imperfect plate. The acoustic radiation is taken into account by using a finite difference approach for the sound field. The vibroacoustic coupling gives rise to a complete model which is applied for the purpose of sound synthesis of cymbals and gong-like instruments. Simulation results are shown in order to investigate the influence of the geometric imperfection on the sound produced. Plates with different profiles are compared and focus is set on the ability of the imperfection to favour the appearance of the turbulent regime.

Keywords: Imperfect plates, Nonlinear vibrations, Sound synthesis I-INCE Classification of Subjects Number(s): 23.1, 41.5

1. INTRODUCTION

Thin plates vibrating with amplitudes comparable to their thickness display a geometric nonlinearity, which is responsible of numerous features such as jump phenomena, hysteretic behaviour or chaotic vibrations. In the field of musical acoustics, the strongly nonlinear regime is responsible for the bright shimmering sound which is typical of gongs and cymbals. In recent years, it has been shown that this regime is turbulent, with the presence of an energy cascade from the large to the small wavelengths [1–4]. One consequence of this strongly nonlinear regime is the difficulty for simulating such dynamics, and thus to sound synthesize percussion instruments such as gongs and cymbals.

Thanks to the progresses in computational methods and in particular to the use of conservative schemes, robust and efficient methods have appeared recently for the sound synthesis of cymbals and gongs [5–8]. This paper is based on the results presented in [8] and proposes two major improvements. First, the case of imperfect plates is tackled. This step is crucial in order to bring the numerical method closer to real cases, and to encompass shallow spherical shells. Second, the acoustic coupling is taken into account, so that a complete vibroacoustic model is finally developped. The numerical model is here used with the purpose of sound synthesis but its peculiar features makes it a perfect candidate for all vibroacoustical simulations of nonlinear imperfect plates. In this contribution, the effect of the imperfections on the vibratory part is analyzed, and an example is shown of the results obtained with the complete vibroacoustic model.

2. THEORY AND FORMULATION

In this section, the non-linear equations of motion for perfect and imperfect plates are given. Next, the modal approach used to discretize the problem is described and the temporal conservative scheme for imperfect

[1]email: aragones@ensta.fr
[2]email: cyril.touze@ensta-paristech.fr
[3]email: s.bilbao@ed.ac.uk
[4]email: v1mducce@exseed.ed.ac.uk

plates is presented. Finally, the acoustic radiation of the imperfect plates is summarized.

2.1 General equations

Non-linear vibrations of thin plates can be described using the dynamic analogue of the so-called von Kármán equations, see *e.g.* [8–10] and references therein. For an isotropic plate of volume density ρ, Young modulus E and Poisson ratio ν and after adding the external input force p and the viscous damping c terms, these equations read

$$\rho h\ddot{w} + D\Delta\Delta w = \mathcal{L}(w, F) + p(r, \theta, t) - c\dot{w}, \tag{1a}$$

$$\Delta\Delta F = -\frac{Eh}{2}\mathcal{L}(w, w). \tag{1b}$$

In these equations, w is the transverse displacement at point (r, θ) and $\dot{w}$ and $\ddot{w}$ correspond respectively to its first and second order time derivatives. $D = Eh^3/12(1-\nu^2)$ stands for the flexural rigidity, Δ for the Laplacian operator and F for the Airy stress function. Finally, $\mathcal{L}$ is known as the von Kármán operator which in polar coordinates writes

$$\mathcal{L}(w, F) = w_{,rr}\left(\frac{F_{,r}}{r} + \frac{F_{,\theta\theta}}{r^2}\right) + F_{,rr}\left(\frac{w_{,r}}{r} + \frac{w_{,\theta\theta}}{r^2}\right) - 2\left(\frac{w_{,r\theta}}{r} - \frac{w_{,\theta}}{r^2}\right)\left(\frac{F_{,r\theta}}{r} - \frac{F_{,\theta}}{r^2}\right) \tag{2}$$

with $(\cdot)_{,\alpha\beta}$ denoting partial derivatives with respect to α and β. Note that the von Kármán operator is responsible for the coupling between transverse and in-plane motions which is the source of the geometric nonlinearity that appears for large amplitude vibrations, *i.e.* as soon as w is of the order of the thickness h.

The validity of these equations is founded on the following assumptions [10, 11]. First, the plate must be thin, i.e. $h \ll a$, with h and a being respectively the thickness and the radius of the plate. Second, the Kirchhoff-Love hypotheses are fulfilled and therefore, the transverse shear can be neglected. Third, the expression of the strain tensor is limited to the second order terms. Finally, in-plane and rotatory inertia are neglected, so that an Airy stress function can be used.

2.2 The case of imperfect plates

In order to extend the use of (1) to imperfect plates, the transverse displacement w is redefined as a combination of two terms,

$$w(r, \theta, t) = w_0(r, \theta) + \tilde{w}(r, \theta, t). \tag{3}$$

The first one w_0 represents the static displacement, i.e. the profile of the imperfection at rest, and the second one $\tilde{w}$ corresponds to the dynamic displacement with respect to w_0. This expression is introduced in (1) leading to [10, 12, 13]

$$\rho h\ddot{\tilde{w}} + D\Delta\Delta\tilde{w} = \mathcal{L}(\tilde{w}, F) + \mathcal{L}(w_0, F) + p(r, \theta, t) - c\dot{\tilde{w}}, \tag{4a}$$

$$\Delta\Delta F = -\frac{Eh}{2}\left[\mathcal{L}(\tilde{w}, \tilde{w}) + 2\mathcal{L}(\tilde{w}, w_0)\right]. \tag{4b}$$

By analysing these equations, the effect of the imperfection in the response of the plate can be appraised. On one hand, (4b) shows that F is composed by a quadratic term $\mathcal{L}(\tilde{w}, \tilde{w})$, already present in the perfect plate case, and a linear term $\mathcal{L}(\tilde{w}, w_0)$ which directly depends on the imperfection. This term points out that the imperfection originates a linear coupling between transverse motion and membrane stretching. On the other hand, (4a) contains a cubic and a quadratic term, being the latter function of the imperfection and revealing that the transverse displacement is also dependent on the profile modifications. The appearance of the quadratic nonlinearity is therefore directly connected to the imperfection and the loss of symmetry of the restoring force with respect to the mid-plane. It has for major consequences that second-order internal resonance relationships can be activated. Secondly odd harmonics can also appear in the spectrum of the response. These facts have been used previously in order to show that the imperfction favours the transition to chaotic vibration, when a plate is driven harmonically with a force of increasing amplitude [14, 15].

2.2.1 *Dimensionless form of the equations*

Providing that the quantities involved in the problem are of different orders of magnitude, the variables are often redefined in a dimensionless form:

$$\tilde{w} = h\bar{\tilde{w}},\ w_0 = h\bar{w}_0,\ r = a\bar{r}, \tag{5}$$

$$\tilde{F} = Eh^3\bar{\tilde{F}},\ t = \sqrt{\frac{\rho h a^4}{D}}\bar{t},\ p = \frac{h^4 E}{a^4}\bar{p},\ c = \frac{Eh^3}{2a^2}\sqrt{\frac{\rho h}{D}}\bar{c}. \tag{6}$$

where the bars $\bar{(\cdot)}$ denote dimensionless variables.

Replacing the new definitions in (4) and omitting the overbars to simplify the notation, the equations of motion of the imperfect plate can be rewritten as

$$\ddot{\tilde{w}} + \Delta\Delta\tilde{w} = \varepsilon\left[\mathcal{L}(\tilde{w}, F) + \mathcal{L}(w_0, F) + p(r,\theta,t) - 2c\dot{\tilde{w}}\right], \tag{7a}$$

$$\Delta\Delta F = -\frac{1}{2}\left[\mathcal{L}(\tilde{w}, \tilde{w}) + 2\mathcal{L}(\tilde{w}, w_0)\right] \tag{7b}$$

with $\varepsilon = 12(1-\nu^2)$.

2.3 Modal approach

The discretization of (7) is performed using a modal approach, where $\tilde{w}$ and F are expanded in series in terms of the eigenmodes of the linear system in (1). The modal expansions read

$$\tilde{w}(t,r,\theta) = \sum_{p=1}^{N_\Phi} \frac{\Phi_p(r,\theta)}{\|\Phi_p\|} q_p(t) \tag{8a}$$

$$F(t,r,\theta) = \sum_{p=1}^{N_\Psi} \frac{\Psi_p(r,\theta)}{\|\Psi_p\|} \eta_p(t) \tag{8b}$$

The basis functions $\{\Phi_i\}_{i\in\mathbb{N}}$ and $\{\Psi_i\}_{i\in\mathbb{N}}$ correspond respectively to the transverse and in-plane mode shapes of the perfect plate, obtained from the eigenproblems

$$\Delta\Delta\Phi_i - \omega_i^2\Phi_i = 0, \tag{9a}$$

$$\Delta\Delta\Psi_i - \zeta_i^4\Psi_i = 0. \tag{9b}$$

The boundary conditions are set so that the external loads vanish at the edge of the plate (case of a free edge) [9, 12]. In dimensional form,

$$F \text{ and } w \text{ are bounded at } r = 0, \tag{10a}$$

$$F_{,r} + \frac{1}{a}F_{,\theta\theta} = 0,\ F_{,r\theta} + \frac{1}{a}F_{,\theta} = 0, \text{ at } r = 0 \tag{10b}$$

$$w_{,rr} + \frac{\nu}{a}w_{,r} + \frac{\nu}{a^2}w_{,\theta\theta} = 0, \text{ at } r = a, \tag{10c}$$

$$w_{,rrr} + \frac{1}{a}w_{,rr} - \frac{1}{a^2}w_{,r} + \frac{2-\nu}{a^2}w_{,r\theta\theta} - \frac{3-\nu}{a^3}w_{,\theta\theta} = 0, \text{ at } r = a \tag{10d}$$

The mode shapes are normalized so that

$$\iint_S \Phi_p^2 dS = 1,\ \iint_S \Psi_p^2 dS = 1. \tag{11}$$

with S standing for the plate surface. One main advantage of the circular case relies in the fact that solutions to (9) are analytic (combination of Bessel functions). Analytical expressions are completely given in [8, 9], for the eigenfrequencies ω_i^2 and ζ_i^4, as well as for the mode shapes $\{\Phi_i\}_{i\in\mathbb{N}}$ and $\{\Psi_i\}_{i\in\mathbb{N}}$. This has for consequence that all the linear parameters can be easily computed with the desired accuracy, for a reasonable

computational cost. This is not the case for all other cases, *e.g.* rectangular plate with free edges, where one has to resort to a numerical solution for the linear problem.

The eigenmodes of the circular plate are denoted by the number of nodal diameters k and the number of nodal circles n, i.e. (k, n). Thus, modes with $k = 0$ are axisymmetric.

Finally, the imperfection profile w_0 is projected onto the transverse vibration modes,

$$w_0(r,\theta) = \sum_{p=1}^{N_0} \frac{\Phi_p(r,\theta)}{\|\Phi_p\|} a_p + z_g \tag{12}$$

where the projection coefficients a_p and the center of mass' offset z_g are obtained thanks to the orthogonality property of the eigenmodes,

$$a_p = \iint_S w_0 \Phi_p dS, \tag{13}$$

$$z_g = \frac{\iint_S w_0}{\pi a^2}. \tag{14}$$

Next, (7a) and (7b) are multiplied respectively by Φ_s and Ψ_s and integrated over the plate surface S, leading to the following temporal system of Ordinary Differential Equations (ODEs),

$$\ddot{q}_s + \omega_s^2 q_s + 2c\dot{q}_s = \varepsilon \left[\sum_{k=1}^{N_\phi} \sum_{l=1}^{N_\phi} E_{kl}^s (q_k + a_k)\eta_l + p_s(t) \right] \tag{15a}$$

$$\eta_l = -\frac{1}{\zeta_l^4} \sum_{m,n}^{N_\Phi} H_{mn}^l \left(q_m q_n + 2 q_m a_n \right). \tag{15b}$$

The previous equations introduce the notation for the non-linear coupling coefficients

$$E_{kl}^s = \int_S \Phi_s \mathcal{L}\left(\Psi_k, \Psi_l\right) dS, \tag{16a}$$

$$H_{mn}^l = \int_S \Psi_l \mathcal{L}\left(\Phi_m, \Phi_n\right), \tag{16b}$$

which quantify the coupling between the transverse modes and the in-plane modes. In some cases, depending on the boundary conditions, $E_{kl}^s = H_{ks}^l$ [8, 10]. This is the case of the present problem and thus, this symmetry condition will be assumed in the reminder of the paper.

A closed form for the transverse modes displacements can be written if (16b) is included in (16a),

$$\ddot{q}_s + \omega_s^2 q_s + 2c\dot{q}_s = -\varepsilon \left[\sum_{k,m,n=1}^{N_\phi} \sum_{l=1}^{N_\phi} \frac{E_{kl}^s H_{mn}^l}{2\zeta_l^4} (q_k + a_k)(q_m q_n + 2 q_m a_n) + p_s(t) \right] \tag{17}$$

and motivates the introduction of the cubic coefficient [8, 12]

$$\Gamma_{kmn}^s = \sum_{l=1}^{N_\phi} \frac{E_{kl}^s H_{mn}^l}{2\zeta_l^4}. \tag{18}$$

2.4 Eigenfrequencies of the imperfect plate

The projection of the imperfect plate onto the perfect plate eigenmodes permits the obtention of the eigenfrequencies of the former in a straightforward manner [12]. Let $\mathbf{A} = \{\varepsilon \alpha_m^s + \omega_s^2 \delta_{sm}\}$ denote the linear part of (17) in matrix form with

$$\alpha_m^s = \sum_{m}^{N_\Phi} \sum_{n}^{N_\Phi} 2\Gamma_{kmn}^s a_k a_n, \tag{19}$$

and δ_{sm} the usual Kronecker delta symbol.

The diagonalization of $\mathbf{A}$ by means of

$$\{\Omega_s \delta_{sk}\}_{s,k\in[1,N_\Phi]} = \mathbf{P}^{-1}\mathbf{A}\mathbf{P} \tag{20}$$

provides the eigenfrequencies of the imperfect plate in Ω_s and the mode shapes in $\mathbf{P}$.

Note that the variation of the imperfect plate's eigenfrequencies with respect to the perfect plate not only depends on the size of the imperfection, but also on the coupling coefficients that involve the projected modes.

2.5 Conservative finite difference scheme

In this section, an energy-conserving scheme for imperfect plates introduced in [5] and adapted for the perfect plate case in [8] is adapted to imperfect plates. The method introduces a set of operators which act on a state vector $\mathbf{q}(n)$ at time step n. First, backward e_{t-} and forward e_{t+} shift operators

$$e_{t-}\mathbf{q}(n) = \mathbf{q}(n-1), \;\; e_{t+}\mathbf{q}(n) = \mathbf{q}(n+1). \tag{21}$$

Backward δ_{t-}, centered $\delta_{t\cdot}$ and forward δ_{t+} approximations to first order time derivatives,

$$\delta_{t-} \equiv \frac{1}{k}(1 - e_{t-}), \;\; \delta_{t\cdot} \equiv \frac{1}{2k}(e_{t+} - e_{t-}), \;\; \delta_{t+} \equiv \frac{1}{k}(e_{t+} - 1), \tag{22}$$

where $k = 1/f_s$ is the time step corresponding to the sampling frequency f_s. They can be combined to obtain an approximation to the second order derivative δ_{tt},

$$\delta_{tt} \equiv \delta_{t+}\delta_{t-} = \frac{1}{k^2}(e_{t+} - 2 + e_{t-}). \tag{23}$$

Finally, the backward μ_{t-}, centered $\mu_{t\cdot}$ and forward μ_{t+} averaging operators are also introduced as

$$\mu_{t-} \equiv \frac{1}{2}(1 + e_{t-}), \;\; \mu_{t\cdot} \equiv \frac{1}{2k}(e_{t+} + e_{t-}), \;\; \mu_{t+} \equiv \frac{1}{k}(e_{t+} + 1). \tag{24}$$

Making use of the previous operators, the temporal conservative scheme for imperfect plates is built as follows,

$$\delta_{tt}q_s(n) + \omega_s^2 q_s(n) + 2c\dot{q}_s = \varepsilon\left[\sum_{k=1}^{N_\phi}\sum_{l=1}^{N_\phi} H_{ks}^l (q_k(n) + a_k)\mu_{t\cdot}\eta_l(n) + p_s(n)\right] \tag{25a}$$

$$\mu_{t-}\eta_l(n) = -\frac{1}{\zeta_l^4}\sum_{i,j}^{N_\Phi} H_{ij}^l \left(q_i(n)e_{t-}q_j(n) + 2a_j\mu_{t-}q_i(n)\right). \tag{25b}$$

The proof that this scheme is energy-conserving can be found in [8]. Note that the scheme is conditionnally stable with the following stability condition to be fulfilled : $f_s \geq \pi f_{N_\Phi}$, where f_{N_Φ} refers to the largest eigenfrequency retained in the truncation for transverse motions [8].

2.6 Acoustic sound synthesis

For the sake of completeness, a method to predict the acoustic radiation of the plate is here implemented. A finite difference approach is used to approximate in time and space the sound field around the plate [16]. The plate is placed inside a grided box full of air, the coupling between the plate and the fluid is established and the acoustic wave equation is approximated at every point of the grid. Let us summarize the procedure step by step.

The acoustic 3D wave equation reads

$$\ddot{\psi} = c_0^2\Delta\psi = c_0^2\left[\psi_{,xx} + \psi_{,yy} + \psi_{,xx}\right] \tag{26}$$

where ψ is the velocity potential, c_0^2 is the air wavespeed and $\Delta = \left(\frac{d^2}{dx^2} + \frac{d^2}{dy^2} + \frac{d^2}{dz^2}\right)$ is the 3D Laplacian operator in Cartesian coordinates. The velocity potential is related to pressure p and particle velocity v by

$$p = \rho\dot{\psi}, \tag{27a}$$

$$v = -\nabla\psi. \tag{27b}$$

where ∇ is the 3D gradient.

Next, the velocity potential is discretized throughout the grid such that

$$\psi^n_{l,m,p} \cong \psi(lh, mh, ph, nh_s), \qquad \text{for } \; l,m,p \in [1,N]^3\,, \tag{28}$$

where $\psi^n_{l,m,p}$ stands for the velocity potential at timestep n and discrete point l, m, p, with h_s corresponding to the grid spacing, $k = 1/f_s$ to the time step and N to the number of points at every dimension of the grid. The sampling frequency f_s is set to match the one used in the modal plate model. The grid spacing is chosen so that the stability condition,

$$\lambda = \frac{c_0^2 k^2}{h_s^2} \leq \frac{1}{\sqrt{3}}, \tag{29}$$

is satisfied [17, 18]. The second order time derivative of the velocity potential is approximated at every point of the grid using

$$\ddot{\psi} \cong \frac{1}{k^2}\left[\psi^{n+1}_{l,m,p} - 2\psi^n_{l,m,p} + \psi^{n-1}_{l,m,p}\right], \tag{30}$$

and the second order spatial derivatives,

$$\psi_{xx} \cong \frac{1}{h_s^2}\left[\psi^n_{l+1,m,p} - 2\psi^n_{l,m,p} - \psi^n_{l-1,m,p}\right], \tag{31a}$$

$$\psi_{yy} \cong \frac{1}{h_s^2}\left[\psi^n_{l,m+1,p} - 2\psi^n_{l,m,p} - \psi^n_{l,m-1,p}\right], \tag{31b}$$

$$\psi_{zz} \cong \frac{1}{h_s^2}\left[\psi^n_{l,m,p+1} - 2\psi^n_{l,m,p} - \psi^n_{l,m,p-1}\right]. \tag{31c}$$

The boundary conditions correspond to the first-order Engquist-Majda absorbing boundary conditions developed in [19].

Replacing (31) and (30) in (26), the velocity potential is obtained as

$$\psi^{n+1}_{l,m,p} = \frac{2}{1+b\lambda/2}\psi^n_{l,m,p} - \frac{1-b\lambda/2}{1+b\lambda/2}\psi^{n-1}_{l,m,p} + \frac{\lambda^2}{1+b\lambda/2}\left[\sum_{\{(l_i,m_i,p_i)\}\in N_n} \psi^n_{l_i,m_i,p_i} - (6-b)\psi^n_{l,m,p}\right] \tag{32}$$

where N_n is the set of neighbours in the box of point (l, m, p) and $b = |N_n|$ is the number of neighbours of the mentioned point.

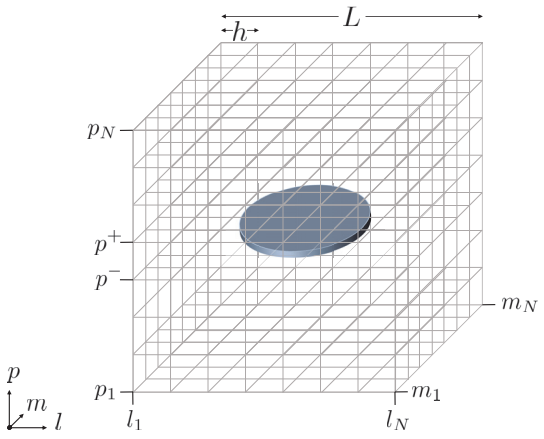

Figure 1. 3D grid for audio synthesis.

The plate is then placed in the center of the box, between p^- and p^+, and discretized to match the 3D grid as shown in Figure 1. As a first approximation, the imperfection of the plate H is assumed to be smaller than the grid space h_s, i.e. $H < h_s$.

The coupling between the plate and the air is done by using the plate velocity as the excitation of the air inside the box. Assuming that the velocity of the plate at every point of the grid can be approximated

using only the normal component, the velocity potential at the points immediately over and below the plate is computed as

$$\psi_{l,m,p^+}^{n+1} = 2\psi_{l,m,p^+}^{n} - \psi_{l,m,p^+}^{n-1} + \lambda^2 \left[\sum_{\{(l_i,m_i,p_i)\}\in N_n^+} \psi_{l_i,m_i,p_i}^{n} - 5\psi_{l,m,p^+}^{n} \right] + \frac{c_0^2 k^2}{h_s^2} v_{l,m} \tag{33a}$$

$$\psi_{l,m,p^-}^{n+1} = 2\psi_{l,m,p^-}^{n} - \psi_{l,m,p^-}^{n-1} + \lambda^2 \left[\sum_{\{(l_i,m_i,p_i)\}\in N_n^-} \psi_{l_i,m_i,p_i}^{n} - 5\psi_{l,m,p*-}^{n} \right] - \frac{c_0^2 k^2}{h_s^2} v_{l,m} \tag{33b}$$

where $N_n^+ = N_n - (l,m,p^-)$, $N_n^- = N_n - (l,m,p^+)$ and $v_{l,m}$ is the transverse velocity of the plate at point (l,m).

Finally, the acoustic pressure at every point of the grid is obtained from

$$p_{l,m,p}^{n} = \frac{\rho_0}{k} \left[\psi_{l,m,p}^{n} - \psi_{l,m,p}^{n-1} \right]. \tag{34}$$

3. SIMULATION RESULTS

The aim of this section is to compare the response of the plate depending on the imperfection profile and the position of the excitation. The plate used for the numerical tests consists of a 84" gong-like circular plate of radius $a = 0.4318$ m, thickness $h = 1 \times 10^{-3}$ m and made of an isotropic homogeneous material with mass density $\rho = 7860$ kg/m^3, Poisson ratio $\nu = 0.38$ and Young modulus $E = 200$ GPa. The damping coefficient is mode dependent and follows a power law, *i.e.* $c_s = 0.008\omega_s^{0.6}$, following [8, 20].

The excitation is selected to represent the strike of a mallet on a point of the gong. The simplest approximation consists of a pointwise excitation at point $\mathbf{x}_0 = (\theta, r)$ given by

$$p(\mathbf{x} - \mathbf{x}_0) = \delta(\mathbf{x} - \mathbf{x}_0) g(t) \tag{35}$$

where $g(t)$ is a raised cosine time signal,

$$g(t) = \begin{cases} \frac{p_m}{2} \left[1 + cos\left(\frac{\pi(t-t_0)}{T_{wid}} \right) \right], & \text{if } |t - t_0| \leq T_{wid} \\ 0, & \text{if } |t - t_0| > T_{wid}, \end{cases} \tag{36}$$

with p_m standing for the force amplitude and T_{wid} for half the interaction time of the pulse.

The modal truncation in (25) is set to 1000 transverse modes, with $f_{1000} = 5086.7$ Hz. The number of in-plane modes is truncated to 60, a sufficient number to ensure convergence of the nonlinear coefficients [8]. The sampling rate is set to $f_s = 31.96$ kHz so that the the stability of the scheme together with sufficient accuracy for the upper modes is fulfilled. The simulation time is set to $T_s = 5$ s to cover the strike and the dissipation of the main part of the energy.

For the results presented in this section, the emphasis is put on the vibratory part. Hence, the analyzed output is selected as the displacement at an arbitrary point of the plate at $\mathbf{x}_o = (0.5192, 0.8962a)$.

3.1 Comparison in terms of the excitation point

The first case investigated considers a perfect plate with varying excitation point, in order to understand and calibrate the influence of the striking point on the plate vibration. The first excitation point, $\mathbf{x}_{0,1} = (0,0)$ is set at the center of the plate in order to excite uniquely the axisymmetric modes of the plate. The second excitation point $\mathbf{x}_{0,2} = (\pi/127, 0.1a)$ is located close to the center to excite mostly axisymmetric modes but including some other modes as well. Finally, the third excitation $\mathbf{x}_{0,3} = (\pi/4, 0.92a)$ point is set close to the edge of the plate and selected to excite the maximum possible number of modes. The amplitude of the force is $p_m = 300N$ and half the interaction time $T_{wid} = 5$ ms.

The spectrograms of the displacement at the output point are shown in Figure 3.1. The first figure on the left, Fig. 2(a), corresponds to the excitation at center. It can be observed that the vibration is almost linear as all eigenfrequencies appear almost distinctively in the spectrum. In the second case, Fig. 2(b), couplings begins to appear, and are finally fully activated for the strike at the edge, Fig. 2(c), where a clear build-up of

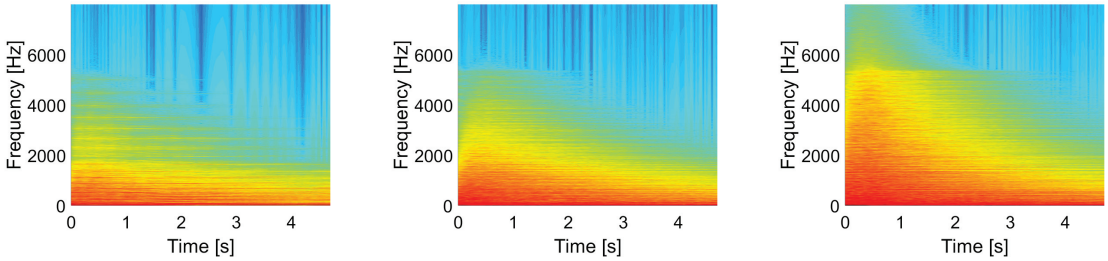

(a) $\mathbf{x}_{0,1} = (0, 0)$ (b) $\mathbf{x}_{0,2} = (\pi/127, 0.1a)$ (c) $\mathbf{x}_{0,3} = (\pi/4, 0.92a)$

Figure 2: Spectrograms corresponding to the displacement at the selected output point $\mathbf{x}_o$, for different position of the input force, respectively at center, $\mathbf{x}_{0,1} = (0, 0)$; near center, $\mathbf{x}_{0,2} = (\pi/127, 0.1a)$; and close to the edge, $\mathbf{x}_{0,3} = (\pi/4, 0.92a)$. Perfect plate with $p_m = 300$ N and $T_{wid} = 5$ ms.

energy is present in the spectrogram, indicating that the turbulent behaviour is at hand with energy cascading in the first milliseconds from the frequency content of the excitation up to 6000 Hz.

These simulations indicate that when the excitation is perfectly at the center point, such that only axisymmetric modes are excited by the external force, no energy is transferred to the whole spectrum. This is the consequence of the fact that, due to symmetry reasons, coupling coefficients between axisymmetric and asymmetric modes are vanishing for the perfect plate [9]. This theoretical case disappears as soon as the striking point is not perfectly at center. It should also disappear with an imperfection in the plate, which is unavoidable in real plates. However, in the case of an axisymmetric imperfection, this rule on the coupling coefficients should continue since the axial symmetry is not broken. This will be investigated in the next subsections.

3.2 Comparison in terms of the imperfection profile

In this section, the effect of the imperfection on the vibratory response of nonlinear plates is investigated. Two different imperfection profiles are selected for that purpose.

3.2.1 Imperfections proportional to mode $(0, 1)$

The first imperfection is shown in Figures 3(a) and 3(c). Its profile is proportional to the first axisymmetric mode shape of the perfect plate, i.e. mode $(0, 1)$, so that the approximated w_0 is expressed by a single coefficient $a_{(0,1)}$. In this case, $H = 2a_{(0,1)}$. The values of this coefficient, $a_{(0,1)} = \{0.36h, 1.73h, 2.02h\}$, are set so that the eigenfrequencies of the plates satisfy the relationships gathered in Table 1. The presence of such relationships favours the couplings between modes via *internal resonance*, and thus the energy transfer between the modes of the structure in order to attain more easily the turbulent behaviour.

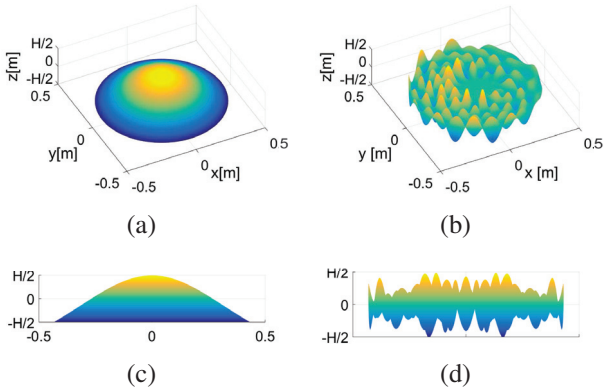

Figure 3: 3D views and profile sections of the test imperfections. (a),(c) Imperfection proportional to mode (0,1); (b),(d) Asymmetric imperfection.

Table 1. Relationships between the eigenfrequencies

$a_{(0,1)} = 0.36h$	$a_{(0,1)} = 1.73h$	$a_{(0,1)} = 2.02h$
$2\omega_{(2,0)} \simeq \omega_{(0,1)}$	$2\omega_{(3,0)} \simeq \omega_{(0,1)}$	$\omega_{(4,0)} \simeq \omega_{(5,0)}$
$2\omega_{(0,1)} \simeq \omega_{(1,1)}$	$2\omega_{(0,1)} \simeq \omega_{(0,2)}$	$\omega_{(3,0)} + \omega_{(1,1)} \simeq \omega_{(5,0)}$
	$\omega_{(3,0)} + \omega_{(5,0)} \simeq \omega_{(6,0)}$	$\omega_{(2,0)} + \omega_{(0,1)} \simeq \omega_{(5,0)}$

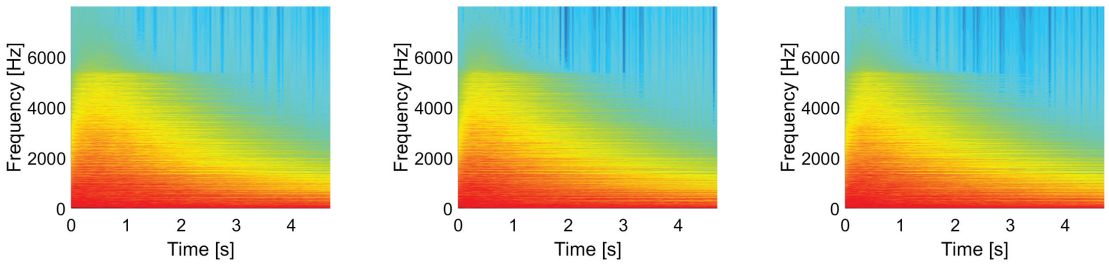

(a) $a_{(0,1)} = 0.36h$ (b) $a_{(0,1)} = 1.73h$ (c) $a_{(0,1)} = 2.02h$

Figure 4. Spectrograms corresponding to plates with profile proportional to mode $(0, 1)$.

The spectrograms of the displacement at the output point $\mathbf{x}_o$ when the plate is excited with a pulse of $p_m = 200$ N are plotted in Figure 3.2.1. The excitation point is selected close to the edge, $\mathbf{x}_{0,3} = (\pi/4, 0.92a)$. The three cases show that the turbulent behaviour is activated, and is most pronounced in the third case for $a_{(0,1)} = 2.02h$. Other simulations, not shown in the paper for the sake of brevity, where the excitation force is at center point, show undoubtedly a linear behaviour. This underlines that if the imperfection is axisymmetric, as in the perfect case, the coupling between axisymmetric and asymmetric modes can not be activated. On the other hand, the simulations with the strike close to the edge show the importance of internal resonances in order to attain easily the turbulent regime.

3.2.2 Asymmetric imperfection

The second imperfection profile, plotted in Figures 3(b) and 3(d) is fully asymmetric in order to observe the effect of breaking the axial symmetry of the system. This shape is obtained as the combination of three asymmetric modes, i.e. $w_0 \approx -0.1029\Phi_{(9,3)} + 0.1471\Phi_{(11,5)} - 0.1324\Phi_{(12,5)}$, with $H = 1h$.

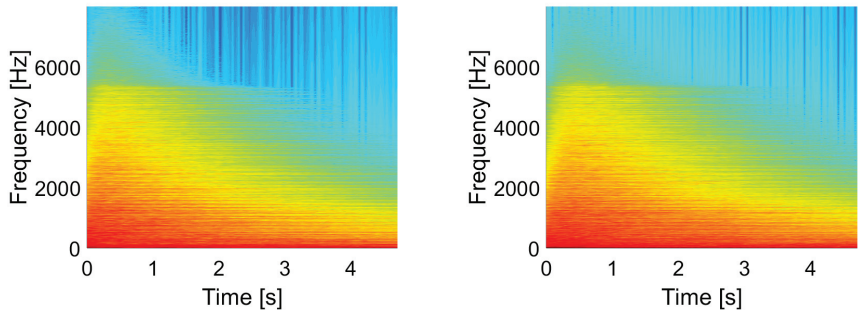

(a) $\mathbf{x}_{0,1} = (0, 0)$, $p_m = 500$ N (b) $\mathbf{x}_{0,2} = (\pi/4, 0.92)$, $p_m = 200$ N

Figure 5: Spectrograms of output point $\mathbf{x}_o$, for the asymmetric imperfection shown in Fig. 3(b) and 3(d). The striking point is respectively at center, $\mathbf{x}_{0,1} = (0, 0)$ (left), and close to the edge, $\mathbf{x}_{0,2} = (\pi/4, 0.92)$ (right).

The response of the plate is evaluated when hit at the center and close to the edge. In this case, results are shown for two different input values, Figure 5(a) shows the spectrogram of the displacement at the output point for an input of $p_m = 500$ N at $\mathbf{x}_{0,1} = (0, 0)$ whereas Figure 5(b) plots the same magnitude when the plate is hit at $\mathbf{x}_{0,2} = (\pi/4, 0.92)$ with $p_m = 200$ N. The main observation is that with the asymmetric imperfection, couplings are now activated when the plate is stricken at center. This shows that, by breaking

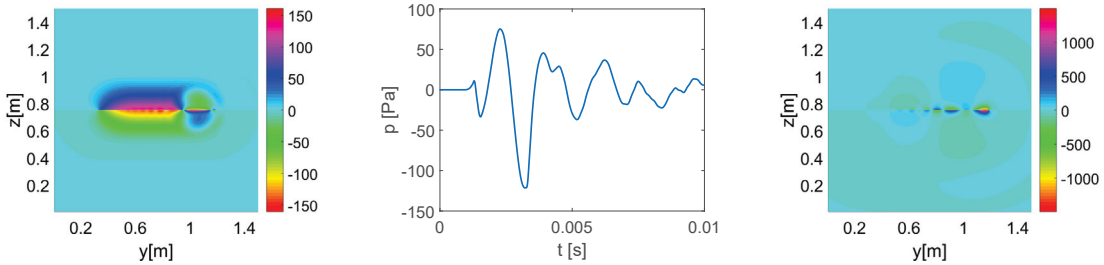

(a) (b) (c)

Figure 6: Acoustic pressure obtained with the sound synthesis method. (a) At ZY-plane section at $X = 0.75$ m and $t = 1.1$ ms. (b) At point $(0.75, 0.94, 1.03)$. (c) At ZY-plane section at $X = 0.75$ m and $t = 2.2$ ms.

the axial symmetry, coupling coefficients are now non vanishing, so that energy can be easily exchanged between the modes to attain the turbulent behaviour. Nevertheless, a larger amount of input energy is needed in the case of the strike at center, in order to obtain the same maximal cut-off frequency at the end of the cascading regime. Indeed, in Figs. 5(a) and 5(b), the cascade excites a high frequency content up to 4000 Hz, but for two different values of the input force p_m.

3.3 Application of sound synthesis

In order to illustrate the full vibroacoustic model, the sound synthesis method is applied to a plate with a spherical profile of $H = h$. Since the radius of the plate is $a = 0.4318$ m, the side of the box is set $L = 1.5$ m. The sampling frequency is $f_s = 100$ kHz and λ is set so that $h_s = 0.0038$. The modal series is truncated to 1000 modes to ensure a response up to 15 kHz. The plate is excited with a raised cosine of $p_m = 300$ N and $T_{wid} = 1$ ms at point $\mathbf{x}_0 = (\pi/4, 0.92)$ and time $T_0 = 0.1$ ms. This means that the input signal reaches its maximum at $t = 1.1$ ms. Figure 6(a) shows the acoustic pressure at plane $X = 0.75$ m at time of maximum input energy, i.e. $t = 1.1$ ms. Next, the pressure is plotted for a single point $(x_b, y_b, z_b) = (0.75, 0.94, 1.03)$ for the first 10 ms. One can observe that the maximum peak of this signal is located at $t = 2.2$ ms, reflecting the delay between the plate response and the acoustic pressure at that point is $\Delta t = 1.1$ ms. Figure 6(c) shows the acoustic pressure at the same plane than Fig 6(b) but at time $t = 2.2$ ms, corresponding to the time of maximum pressure at (x_b, y_b, z_b). The advantage of the sound synthesis method is that it provides the global response of the plate together with the radiated sound pressure, contrary to the dynamic method where only pointwise results are obtained.

4. CONCLUSIONS

In this paper, a complete vibroacoustic modelling for the sound synthesis of imperfect nonlinear circular plates, has been derived. The main features of the numerical methods used are: (i) a modal approach for the nonlinear vibratory part, in order to be able to implement any frequency-dependent damping law, (ii) a conservative time-marching scheme and (iii) a finite difference radiation method in order to compute the coupled vibroacoustic problem.

Several cases of study have been implemented to discuss the influence of the excitation point and the imperfection profile on the strongly nonlinear, turbulent response of plates, showing in particular the importance of internal resonance relationships, together with asymmetric imperfection in order to break the axial symmetry and activate the largest number of couplings between modes.

These results are very important with regard to sound synthesis of cymbals and gong-like instruments. It gives a unified framework for solving the complete vibroacoustic problem, with the simulation of realistic sounds, in particular thanks to the modal approach. Strongly nonlinear regime with turbulent behaviour are also easily synthesized, with a reasonable computational burden. Finally, taking into account the imperfection is very important in order to simulate real cases.

5. ACKNOWLEDGEMENTS

The research work presented in this paper has been funded by the European Commission within the Initial Training Network (ITN) Marie Curie action project BATWOMAN, under the Seventh Framework Program (EC grant agreement no. 605867).

REFERENCES

[1] G. Düring, C. Josserand, and S. Rica. Weak turbulence for a vibrating plate: Can one hear a Kolmogorov spectrum? *Physical Review Letters*, 97:025503, 2006.

[2] A. Boudaoud, O. Cadot, B. Odille, and C. Touzé. Observation of wave turbulence in vibrating plates. *Physical Review Letters*, 100:234504, 2008.

[3] M. Ducceschi, O. Cadot, C. Touzé, and S. Bilbao. Dynamics of the wave turbulence spectrum in vibrating plates: A numerical investigation using a conservative finite difference scheme. *Physica D*, 280-281:73–85, 2014.

[4] O. Cadot, M. Ducceschi, T. Humbert, B. Miquel, N. Mordant, C. Josserand, and C. Touzé. Wave turbulence in vibrating plates. In C. H. Skiadas and C. Skiadas, editors, *Handbook of applications of chaos theory*. Chapman and Hall/CRC, 2016.

[5] S. Bilbao. A family of conservative finite difference schemes for the dynamical von karman plate equations. *Numerical Methods for Partial Differential Equations*, 24(1):193–216, 2008.

[6] S. Bilbao. Percussion synthesis based on models of nonlinear shell vibration. *IEEE Transactions on Audio, Speech and Language Processing*, 18(4):872–880, 2010.

[7] J. Chadwick, S. An, and D. James. Harmonic shells: a practical nonlinear sound model for near-rigid thin shells. *ACM Transactions on Graphics (SIGGRAPH ASIA Conference Proceedings)*, 28(5):Article 119, 2009.

[8] M. Ducceschi and C. Touzé. Modal approach for nonlinear vibrations of damped impacted plates: Application to sound synthesis of gongs and cymbals. *Journal of Sound and Vibration*, 344:313–331, 2015.

[9] C. Touzé, O. Thomas, and A. Chaigne. Asymmetric non-linear forced vibrations of free-edge circular plates. part 1: Theory. *Journal of Sound and Vibration*, 258(4):649–676, 2002.

[10] O. Thomas and S. Bilbao. Geometrically nonlinear flexural vibrations of plates: In-plane boundary conditions and some symmetry properties. *Journal of Sound and Vibration*, 315(3):569–590, 2008.

[11] C.Y. Chia. *Nonlinear analysis of plates*. McGraw-Hill International Book Company, 1980.

[12] C. Camier, C. Touzé, and O. Thomas. Non-linear vibrations of imperfect free-edge circular plates and shells. *European Journal of Mechanics-A/Solids*, 28(3):500–515, 2009.

[13] G. L. Ostiguy and S. Sassi. Effects of initial geometric imperfections on dynamic behavior of rectangular plates. *Nonlinear Dynamics*, 3(3):165–181, 1992.

[14] C. Touzé, O. Thomas, and M. Amabili. Transition to chaotic vibrations for harmonically forced perfect and imperfect circular plates. *International Journal of Non-linear Mechanics*, 46(1):234–246, 2011.

[15] C. Touzé, S. Bilbao, and O. Cadot. Transition scenario to turbulence in thin vibrating plates. *Journal of Sound and Vibration*, 331(2):412–433, 2012.

[16] S. Bilbao. Time domain simulation and sound synthesis for the snare drum. *The Journal of the Acoustical Society of America*, 131(1):914–925, 2012.

[17] S. Bilbao. *Numerical Sound Synthesis: Finite Difference Schemes and Simulation in Musical Acoustics*. John Wiley & Sons, 2009.

[18] A. Torin and S. Bilbao. A 3d multi-plate environment for sound synthesis. In *Proceedings of the 16th International Digital Audio Effects Conference (Maynooth, Ireland)*, 2013.

[19] B. Engquist and A. Majda. Absorbing boundary conditions for numerical simulation of waves. *Proceedings of the National Academy of Sciences*, 74(5):1765–1766, 1977.

[20] T. Humbert, O. Cadot, G Düring, C. Josserand, S Rica, and C. Touzé. Wave turbulence in vibrating plates: The effect of damping. *EPL (Europhysics Letters)*, 102(3):30002, 2013.